An Inverter Circuit Configuration Suitable for Vessels of Different Material for Multiload Induction Cooking Application

Bhavin Salvi, S. Porpandiselvi, *Member, IEEE*, and N. Vishwanathan

***Abstract*— In heating applications, induction heating (IH) is a dominant technology in the market due to several advantages over conventional heating techniques. Most of the research in the past has focused on heating ferromagnetic (FM) material-type vessels. Now, there is an increase in research for proposing topologies suitable for heating FM and non-FM (N-FM) type vessels. In this article, an inverter circuit is proposed for heating FM and N-FM material vessels. A simple ON–OFF control is used for obtaining simultaneous as well as independent control for both loads. It offers linear power control. The range of power control for N-FM load is increased by using frequency-based control. The proposed inverter circuit has been simulated in OrCAD PSpice and experimentally verified with a prototype for 1624 W. It offers a peak experimental efficiency of 94.3%. It can also be extended for multiple loads by adding a low-frequency operated switch and a diode combination for additional IH load. A detailed loss analysis for the proposed inverter has been carried out using PSIM software. The simulation and experimentation results are in good accord with each other. Hence, the proposed inverter circuit is a suitable solution for heating FM and N-FM material vessels for multiload applications.**

***Index Terms*— Frequency control, induction cooking (IC), induction cooking system (ICS), linear power control, multiload, ON–OFF control, resonant inverter circuit.**

I. Introduction

AMONG all the available heating techniques, induction heating (IH) is the most prominent technique due to its multiple advantages. Some of the key advantages of induction heating (IH) technology are cleanliness, better control, safer operation, and quicker heating [1]. It also offers very high efficiency over conventional methods as heat is produced directly in the material to be heated [2]. A good amount of research has been done in the past on developing suitable configuration and power control methods for heating FM loads [2]. In order to heat an FM load, typically a 20–30-kHz frequency range power supply is required. This high-frequency power supply is obtained by rectification and then inverting it to a suitable high-frequency ac for IH. Single switch [3], half-bridge (HB) [4] and full-bridge (FB) [5] are frequently used for IH application. The most commonly used controls techniques for IH are asymmetric duty cycle (ADC) control [6], asymmetric voltage cancellation (AVC) control [7] and phase shift control (PSC) [8].

FM and N-FM loads have different heating requirements [9]. Typically, FM loads offer higher permeability and higher resistivity when operating at a 20–30-kHz range. Hence, sufficient heat can be obtained in FM loads by powering them in this frequency range. On the other hand, N-FM loads offer low permeability and low resistivity for this range of operating frequency. Low resistance in this operating range of frequency would lead to very high currents in the circuit [10], which is not desirable. With an increase in frequency, the resistance of the N-FM load increases. So in order to heat N-FM loads, operating at high frequency is required.

A configuration has been proposed in [11] with load detection control. But this is a bulky and heavy solution. In [12], a double-layer coil solution has been proposed which increases the frequency of the flux produced when two 180-degree phase shifted currents are passed through it. There is complexity in the design. In [10], a selective harmonic approach was used for all metal heating. But the current requirement for N-FM vessel is high. Single frequency double layer coil approach is used in [13]. This reduces the current requirement of the inverter but it has a complex design. Time-sharing technique is used in [14] to meet different material requirements. Load adaptive modulation technique with FB and HB inverters is proposed in [15]. Frequency doubler and tripler modes are used according to the type of material. A dual resonant topology has been proposed in [16]. It uses series and series-parallel resonance for heating FM and N-FM material respectively. But the above three methods use electro-mechanical switches which have their own limitations. Multiphase coupled coil approach is used in [17]. It has drawbacks because of the increased component count and complex design. Cascaded FB topology is used in [18] for heating all metal but it has the drawback of several components. In [19], a simple FB inverter with dual frequency control is proposed. It varies the duty cycle of the bridge which limits the soft-switching operation.

Multiple-load heating is a common requirement for induction cooking (IC) applications. The key requirements of multiple-load IH applications are simultaneous and independent power control for heating different material vessels and

Manuscript received 21 April 2022; revised 18 August 2022 and 13 January 2023; accepted 12 February 2023. Date of publication 22 February 2023; date of current version 13 June 2023. Recommended for publication by Associate Editor Martin Ordonez. *(Corresponding author: Bhavin Salvi.)*

The authors are with the Department of Electrical Engineering, National Institute of Technology Warangal, Warangal 506004, India (e-mail: sbhavin@student.nitw.ac.in).

Color versions of one or more figures in this article are available at https://doi.org/10.1109/JESTPE.2023.3247482.

Digital Object Identifier 10.1109/JESTPE.2023.3247482

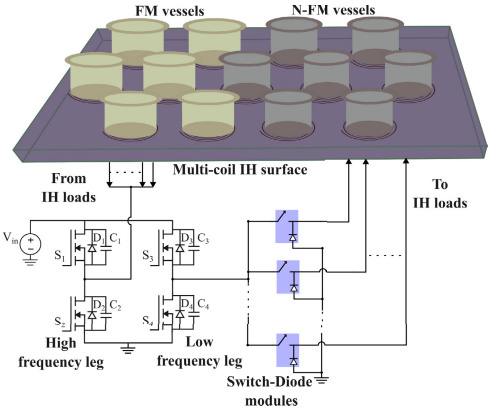

Fig. 1. Proposed scheme for multiload ICS for vessels of different material.

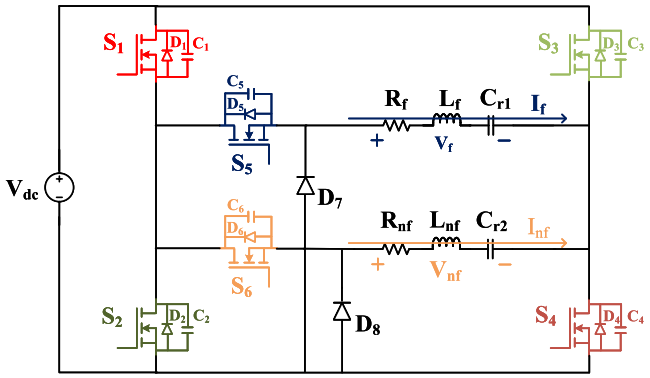

Fig. 2. Proposed inverter configuration.

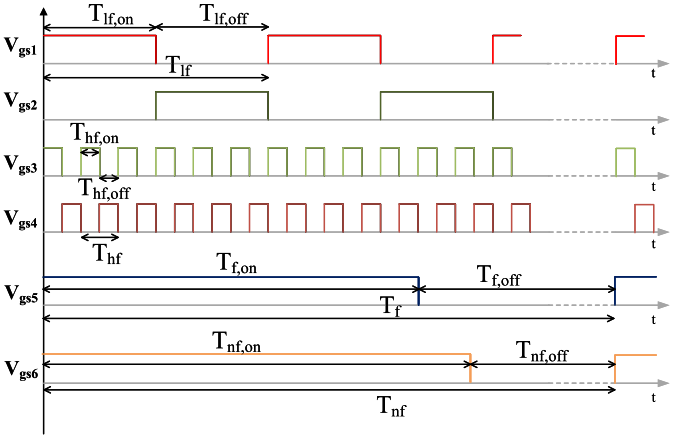

Fig. 3. Gate pulses for the inverter switches.

simple control and easy extension for multiple loads. Traditional HB and FB inverter topologies are not suitable for the above-mentioned requirements. In the literature, different inverter topologies are presented which are mostly for FM loads only. The proposed inverter topology uses a basic FB inverter which can power any number of IC loads with an additional low-frequency operated switching device and a diode for each IC load. In addition to that, the proposed topology is suitable for FM and N-FM IC loads. The proposed scheme for multiple load ICS for vessels of different materials is presented in Fig. 1. Some key features of the proposed IC system solution are as follows.

1) Ability to heat both FM and N-FM loads, independent and simultaneous power control in multiple loads of different materials.
2) Independent and simultaneous power control in multiple loads of different materials.
3) Linear output power regulation with ON–OFF control technique.
4) Possibility for the extension to more than two loads by a series low frequency operated switch and diode combination for each additional IC load.

Further, this article is subdivided into Section II to Section V. Section II describes the proposed inverter circuit, gate pulses, and modes of operation. Section III details the analysis of the inverter and its power control. In Section IV, simulation and experimental results are presented and operation of the proposed circuit is evaluated. Finally, important conclusions for the research work are presented in Section V.

II. Proposed Inverter Circuit

The proposed inverter circuit for different material IC applications is shown in Fig. 2. It comprises of dc source ($V_{\rm dc}$), six MOSFETs (S_1, S_2, S_3, S_4, S_5, S_6), two diodes (D_7, D_8) and two different material IC loads. Ferromagnetic (FM) load is modeled as "R_f, L_f" and is resonated at a frequency $f_{r,lf}$ using resonant capacitor C_{r1}. Non-FM load is modeled as "$R_{\rm nf}$, $L_{\rm nf}$" and is resonated at a frequency $f_{r,\rm hf}$ using resonant capacitor C_{r2}. As depicted in Fig. 2, "V_f, I_f" and "$V_{\rm nf}$, $I_{\rm nf}$" are respective voltages and currents for FM and N-FM loads. The switches (S_1, S_2, S_3, S_4) form two legs of the inverter. Leg-1 devices (S_1, S_2) are operated at a low frequency f_{lf} ($= 1/T_{lf}$), which is required for FM load. Leg-2 devices (S_3, S_4) are operated at a high frequency $f_{\rm hf}$ ($= 1/T_{\rm hf}$), to meet the heating requirement of N-FM load. The powers in these two different loads are controlled using a series switch and a diode combination per load. The switch-diode combinations "S_5, D_7" and "S_6, D_8" are used to obtain independent power control in FM and N-FM loads respectively as shown in Fig. 2.

The gate pulses for the proposed inverter circuit are shown in Fig. 3. Low-frequency gate pulses V_{gs1} and V_{gs2} are used for switching S_1 and S_2 respectively. T_{lf} is the time period of V_{gs1} and V_{gs2}. $T_{lf,\rm on}$ and $T_{lf,\rm off}$ are the on and off-time periods for V_{gs1} and V_{gs2} respectively. High frequency gate pulses V_{gs3} and V_{gs4} are used for switching S_3 and S_4 respectively. $T_{\rm hf}$ is the time period of V_{gs3} and V_{gs4}. $T_{\rm hf,on}$ and $T_{\rm hf,off}$ are the on and off-time periods for V_{gs3} and V_{gs4} respectively. The on-time periods $T_{lf,\rm on}$ and $T_{\rm hf,on}$ are fixed for the entire operation of the inverter, i.e., $T_{lf,\rm on} = T_{lf}/2$ and $T_{\rm hf,on} = T_{\rm hf}/2$. V_{gs5} and V_{gs6} are used for switching S_5 and S_6 respectively. T_f is the time period of V_{gs5} and $T_{\rm nf}$ is the time period of V_{gs6}. $T_{f,\rm on}$ and $T_{f,\rm off}$ are the on and off time periods for V_{gs5}. $T_{\rm nf,on}$ and $T_{\rm nf,off}$ are the on and off time periods for V_{gs6}.

The operating modes of the proposed inverter are shown in Fig. 4. Fig. 4(a)–(j) which correspond to Mode-1 to Mode-10 respectively.

Mode-1: In this mode, switches S_1, S_4, S_5, and S_6 are on. The FM load is powered by a dc source through S_1, S_5, and S_4.

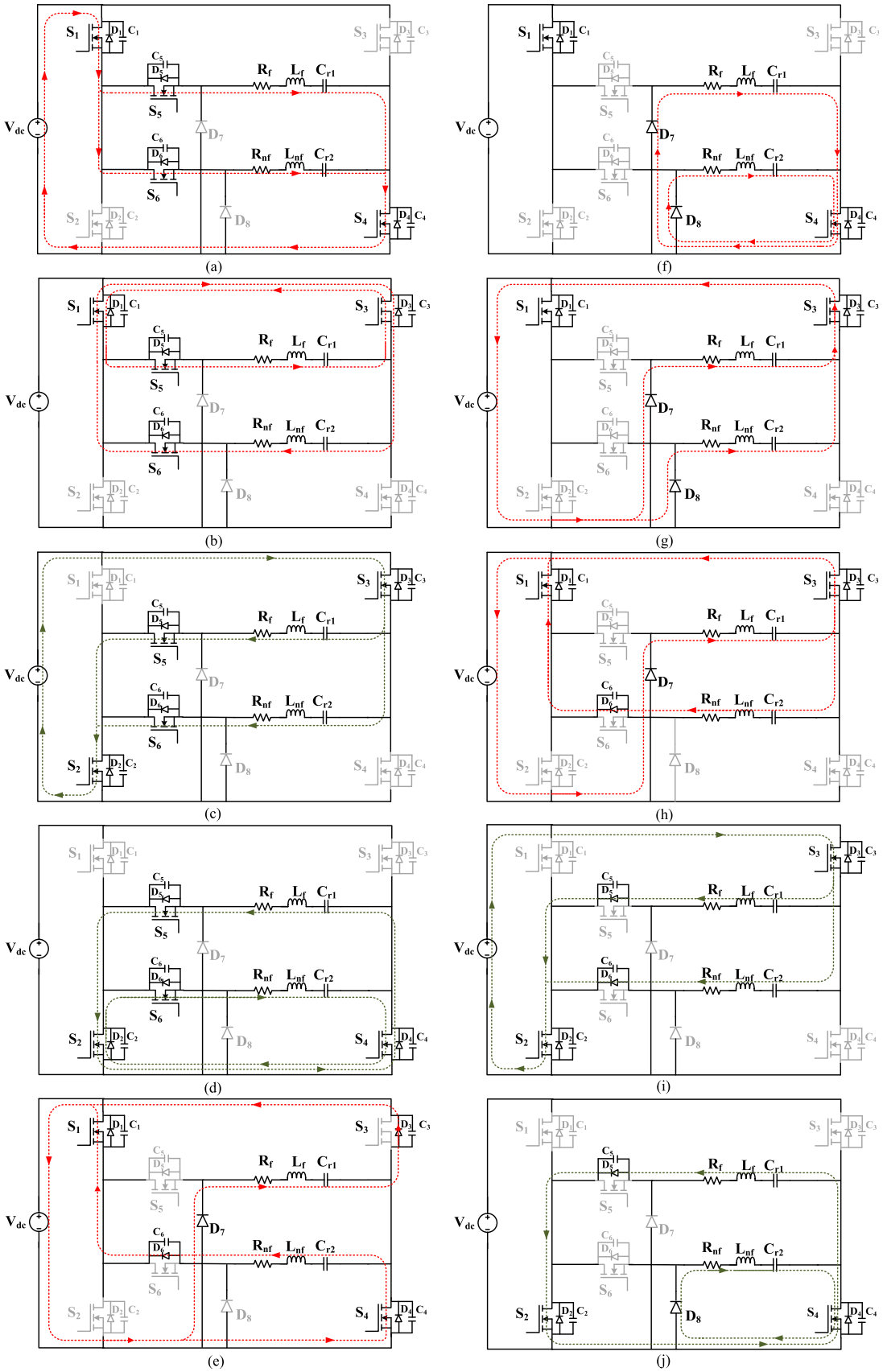

Fig. 4. Operating modes of the proposed inverter. (a)–(j) Mode-1 to Mode-10 respectively.

The N-FM load is powered by a dc source through S_1, S_6 and S_4. The current flow and the state of this mode are shown in Fig. 4(a).

Mode-2: In this mode, both loads are disconnected from the supply as S_4 is turned off. Switches S_1, S_3, S_5, and S_6 are on. FM load is freewheeling through S_1, S_5, and S_3. N-FM load current direction is reversed as the resonant capacitor C_{r2} discharges. The current in N-FM load flows through switches S_6, S_1, and S_3. The state of the circuit for this mode is depicted in Fig. 4(b).

Mode-3: In this mode, both the loads are powered from the supply as S_1 is turned off and S_2 is turned on. The switches S_2, S_3, S_5 and S_6 are on. The FM load is powered by a dc source through S_3, S_5 and S_2. The N-FM load is powered by a dc source through S_3, S_6, and S_2. The direction of the current flow in the FM and N-FM loads is reversed from the previous mode. The current flow and the state of this mode are shown in Fig. 4(c).

Mode-4: In this mode, both loads are disconnected from the supply as S_3 is turned off. Switches S_2, S_4, S_5 and S_6 are on. FM load is freewheeling through S_5, S_2 and S_4. N-FM load current direction is reversed as the resonant capacitor C_{r2} discharges. The current in N-FM load flows through switches S_6, S_2 and S_4. The state of the circuit along with the current flow directions for this mode is depicted in Fig. 4(d).

Mode-5: Switches S_1 and S_4 are on in this mode. FM load current flows through D_3, V_{dc} and D_7. N-FM load current flows through D_6, S_1 and S_4. The flow of currents and the state of the inverter circuit for this mode are shown in Fig. 4(e).

Mode-6: Both loads are freewheeling in this mode. Switches S_1, S_4 and diodes D_7, D_8 are conducing in this mode. FM load is freewheeling through S_4 and D_7. N-FM load is freewheeling through S_4 and D_8. The flow of load currents is shown in Fig. 4(f). The series switches for both loads are off in this mode. As both the series switches are controlled independently, one can be on and the other can be off at the same time. The direction of current will vary depending on the case.

Mode-7: In this mode, switches S_1 and S_3 are on. The current in FM load flows through D_7-S_3-V_{dc}. The magnitude of this current is low as the FM load is tuned to a low frequency. N-FM load current flows through D_8-S_3-V_{dc}. The operating state for this mode is shown in Fig. 4(g).

Mode-8: In this mode, switches S_1 and S_3 are on. FM load current continues to flow as in the previous mode. Resonant capacitor C_{r2} drives the load current through D_6-S_1-S_3. The direction of the current flow and the operating state for the inverter is shown in Fig. 4(h).

Mode-9: In this mode, switches S_2 and S_3 are on. The current in FM load flows through supply V_{dc}-S_3-D_5-S_2. The magnitude of this current will be low as the FM load is tuned to a low frequency. N-FM load is powered by a dc source in this mode. The current flows through dc supply V_{dc}-S_3-D_6-S_2. The operating state of this mode is shown in Fig. 4(i).

Mode-10: In this mode, switches S_2 and S_4 are on. FM load freewheels through D_5-S_2-S_4. Resonant capacitor C_{r2} discharges through S_4-D_8. The direction of the load current flow and the operating state for the inverter is shown in Fig. 4(j).

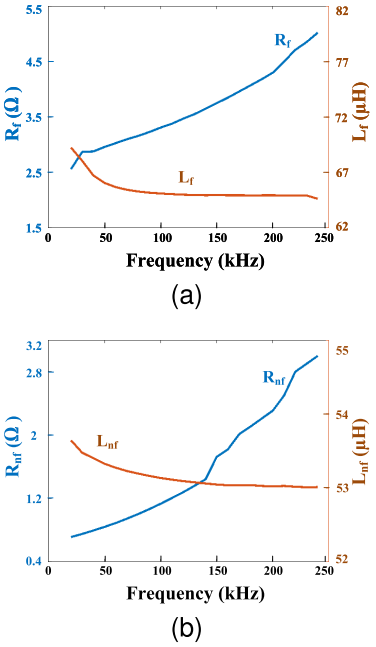

Fig. 5. IC load characteristics with frequency. (a) FM steel load. (b) N-FM aluminum load.

From the different operating modes of the proposed inverter circuit, the following key observations can be made:

1) For Mode-1 to Mode-4, the inverter circuit operates as a full-bridge circuit with two legs operating at different frequencies.
2) By controlling series switches (S_5 and S_6), power can be controlled in both loads independently.
3) Even with a series switch in off condition, during a negative half cycle i.e., when S_3 is on, there is no control over the current. However, current through FM load, in this case, is of very low magnitude as it is tuned to low frequency while $S_3 - S_4$ are switched at high frequency.
4) When the series switch for the N-FM load is off, it gets powered only during the negative half cycle i.e., when S_3 is on. Whereas it discharges when S_3 is turned off and S_4 is on. This leads to variation in current magnitude through N-FM load.

III. Output Power Control

Iron-based materials are categorized as FM materials. Metals that do not contain iron are called N-FM materials like copper, aluminum, lead, etc. For experimentation, FM steel vessels and N-FM aluminum vessels have been selected. The load parameters for the above-mentioned loads are obtained using NumetriQ phase sensitive multimeter-PSM 1735 and the characteristics showing variation of load equivalent inductance and equivalent resistance with operating frequencies are plotted in Fig. 5.

A. Frequency Selection

The operating frequencies of the loads are selected such that they offer nearly equal resistance. From Fig. 5, it is observed

that the equivalent resistance is 2.8 Ω for FM load at 30 kHz and for N-FM load at 220 kHz. Hence, the FM load is operated at 30 kHz and N-FM load is operated at 220 kHz. These two different loads are resonated using series resonant capacitors C_{r1} and C_{r2} respectively such that the loads have resonant frequencies which are a little lower than their respective operating frequencies. The resonant frequencies for FM and N-FM loads respectively can be expressed as

$$f_{r,lf} = \frac{1}{2\pi\sqrt{L_f C_{r1}}} \tag{1}$$

$$f_{r,\mathrm{hf}} = \frac{1}{2\pi\sqrt{L_{\mathrm{nf}} C_{r2}}}. \tag{2}$$

As FM load is tuned at low frequency, it will not respond to high frequency and it offers high impedance for high-frequency component. Similarly, as N-FM load is tuned at high frequency, it does not respond to low frequency and it offers high impedance for low-frequency component.

B. Inverter Analysis

The proposed circuit is analyzed mathematically with the following assumptions: all the components are in their ideal state, the current in FM load is zero when series switch S_5 is off and only fundamental frequency current is present in the loads.

1) FM Load Power: FM load is powered only when its series switch S_5 is on. The fundamental component of the output voltage v_f shown in Fig. 6, can be expressed during ON-state as

$$v_{f,1} = \frac{2V_{\mathrm{dc}}}{\pi}\cos\left(\omega t - \pi\frac{T_{lf,\mathrm{on}}}{T_{lf}}\right). \tag{3}$$

The rms current of the fundamental component can be represented as

$$I_{f1,\mathrm{rms}} = \frac{V_{f1,\mathrm{rms}}}{|Z_{f1}|} = \frac{\sqrt{2}V_{\mathrm{dc}}}{\pi|Z_{f1}|}. \tag{4}$$

The average power responsible for heating steel load is given by

$$P_{\mathrm{st}} = I^2_{f1,\mathrm{rms}} \times R_f \times d_1 = \frac{2(V_{\mathrm{dc}})^2}{\pi^2|Z_{f1}|^2} \times R_f \times D_1 \tag{5}$$

where, d_1 is the duty cycle for ON–OFF control in steel load and is

$$D_1 = \frac{T_{f,\mathrm{on}}}{T_f}. \tag{6}$$

Z_{f1} is the impedance for the fundamental current component in the steel load and can be given as

$$Z_{f1} = R_f + j\left(\omega L_f - \frac{1}{\omega C_{r1}}\right). \tag{7}$$

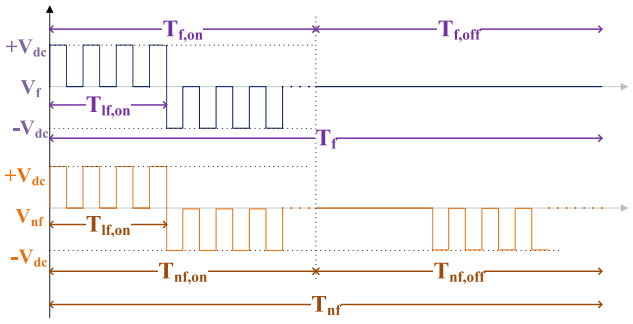

Fig. 6. Approximated load voltage waveforms.

2) N-FM Load Power: N-FM load is powered fully when S_6 is on. When S_6 is turned off, the N-FM load is partially powered. The detailed analysis is described as follows:

When S_6 is on, the output voltage waveform is shown in Fig. 6. The fundamental component of the output voltage v_{nf} shown in Fig. 6, can be expressed during ON-state as

$$v_{\mathrm{nf},1} = \frac{2V_{\mathrm{dc}}}{\pi}\cos\left(\omega t - \pi\frac{T_{\mathrm{hf,on}}}{T_{\mathrm{hf}}}\right). \tag{8}$$

The rms current of the fundamental component is given as

$$I_{\mathrm{nf1,rms}} = \frac{V_{\mathrm{nf1,rms}}}{|Z_{\mathrm{nf1}}|} = \frac{\sqrt{2}V_{\mathrm{dc}}}{\pi|Z_{\mathrm{nf1}}|}. \tag{9}$$

The average power delivered to N-FM load with S_6 on is

$$P_{\mathrm{al,on}} = I^2_{\mathrm{nf1,rms}} \times R_{\mathrm{nf}} \times d_2 = \frac{2(V_{\mathrm{dc}})^2}{\pi^2|Z_{\mathrm{nf1}}|^2} \times R_{\mathrm{nf}} \times D_2 \tag{10}$$

where, d_2 is the duty cycle for ON–OFF control in aluminum load and is given as:

$$D_2 = \frac{T_{\mathrm{nf,on}}}{T_{\mathrm{nf}}}. \tag{11}$$

Z_{nf1} is the impedance for the fundamental component current in the aluminum load and represented as

$$Z_{\mathrm{nf1}} = R_{\mathrm{nf}} + j\left(\omega L_{\mathrm{nf}} - \frac{1}{\omega C_{r2}}\right). \tag{12}$$

During the off duration of S_6, the N-FM load is not powered as long as S_1 is on. During this state, N-FM load is freewheeling and it returns power back to the source for a very short duration. This clamps the output voltage at $\pm V_{\mathrm{dc}}$ which can be observed in the simulation and experimental results. As the average power returned to the source is very low, it is not considered in power calculations. The approximated waveforms are shown in Fig. 6. When S_1 turns off and S_2 is on, the N-FM load is again powered which leads to an increase in load current. Due to the above-mentioned reason, the N-FM load current exhibits an oscillatory envelope ($i_{E,\mathrm{nf}}$) as shown in Fig. 7. The time constant 'τ' of the envelope is ($2L_f/R_f$). Using the detailed approach mentioned in [20], the average

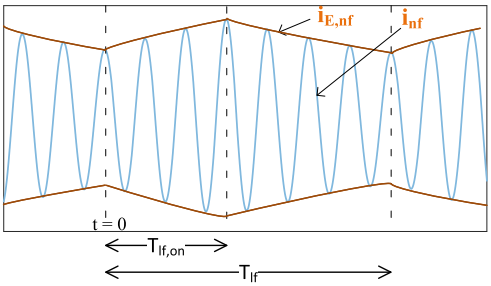

Fig. 7. N-FM load current envelope when S_6 is off.

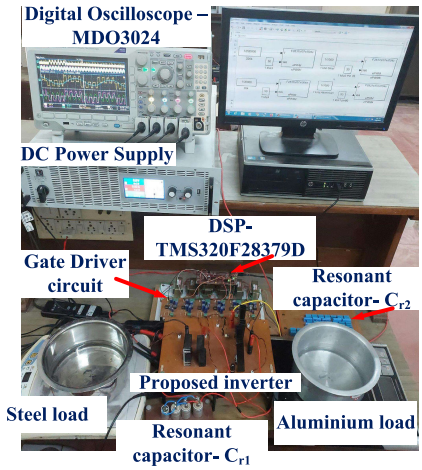

Fig. 8. Laboratory experimentation setup.

power when S_6 is off is given by

$$P_{\text{al,off}} = \left(\frac{V_{\text{dc}}}{\pi}\cos\theta\frac{1}{T_{lf}}\int_0^{T_{lf,\text{on}}} i_{E,\text{nf}}(t)dt\right)\times(1-D_2)$$
$$= \left[P_{\text{al,max}}\frac{T_{lf,\text{on}}}{T_{lf}} + \frac{\tau}{T_{lf}}\left(\frac{1-e^{\frac{-T_{lf,\text{on}}}{\tau}}}{1-e^{\frac{-T_{lf}}{\tau}}}\right)\right.$$
$$\left.\times\left(e^{\frac{-T_{lf,\text{on}}}{\tau}} - e^{\frac{-T_{lf}}{\tau}}\right)\right]\times(1-D_2) \quad (13)$$

where $P_{\text{al,max}} = (1/\pi)V_{\text{dc}}I_{\text{nf1},m}\cos\theta$ is the maximum output power for aluminum when $T_{lf,\text{on}} = T_{lf}$. And θ is the angle between the output voltage and load current. The maximum current can be derived using Fourier analysis and is given by:

$$I_{\text{nf1},m} = \frac{2V_{\text{dc}}}{\pi|Z_{\text{nf1}}|}. \quad (14)$$

Now, using (10) and (13), the total average power responsible for heating the N-FM load (aluminum) is given by

$$P_{\text{al}} = P_{\text{al,on}} + P_{\text{al,off}}. \quad (15)$$

C. Power Control

For the above analysis, the gate pulses for leg-1 and leg-2 switches are operated with fixed duty cycles of 50%. Hence

$$T_{lf,\text{on}} = \frac{T_{lf}}{2}; \quad T_{\text{hf,on}} = \frac{T_{\text{hf}}}{2}. \quad (16)$$

Leg-1 and leg-2 switches are operating at 30 and 220 kHz respectively. From (5) and (13), it can be observed that output powers of both the loads are related to the duty cycles of their respective series switches. So, for the respective load regulation, ON–OFF control is realized by varying respective series switch duty cycles. Series switches S_5 and S_6 are operated at 1 kHz. For FM load, full-range power control is possible using 5. But for N-FM load, some minimum power is present even when the respective duty cycle is zero 13. Hence, for increasing the range of power control, frequency-based control is implemented. By varying the operating frequency of leg-2, the operating point on the respective resonant curve changes as per (2). This leads to a change in the load current. By using this frequency control, the power regulation range is increased for the N-FM load.

TABLE I
PARAMETERS FOR PROPOSED INVERTER CIRCUIT

Component	Value
DC supply voltage, V_{dc}	150V
equivalent resistance of FM load, R_f	2.8 Ω
equivalent inductance of FM load, L_f	65.8 μH
parasitic resistance of FM IH coil, $r_{f,coil}$	90 $m\Omega$
resonant capacitor of FM load, C_{r1}	0.52 μF
equivalent series resistance of C_{r1}, r_{cr1}	6.7 $m\Omega$
equivalent resistance of N-FM load, R_{nf}	2.8 Ω
equivalent inductance of N-FM load, L_{nf}	54.3 μH
parasitic resistance of N-FM IH coil, $r_{nf,coil}$	90 $m\Omega$
resonant capacitor of N-FM load, C_{r2}	10 nF
equivalent series resistance of C_{r2}, r_{cr2}	1.5 $m\Omega$
low switching frequency, f_{lf}	30 kHz
high switching frequency, f_{hf}	220 kHz
load ON-OFF control frequencies, f_{st} and f_{al}	1 kHZ
switching devices, MOSFETs	IRFP4127PbF
drain-source resistance for MOSFETs	17 $m\Omega$
diodes, D_7 and D_8	RURG5060

IV. SIMULATION AND EXPERIMENTATION

The operation of the proposed inverter circuit has been verified through simulation and experiments for the parameters mentioned in Table I. OrCAD PSpice software has been used for simulation. The laboratory experimentation setup for the proposed inverter circuit is presented in Fig. 8. dc source EA-PSI 9750-40 is used for testing the experimental prototype. FM load is realized by using a combination of a steel vessel and an IC coil and it has been modeled as R_f-L_f combination. For the N-FM load, an aluminum vessel and an IH coil are used and it has been modeled as R_{nf}-L_{nf} combination. MKV-B25834 type capacitors are used for realizing resonant capacitor C_{r1}. Series-parallel combinations of MKP-B32672L type capacitors are used for obtaining the required value of C_{r2}. Digital signal processor-TMS320F28379D is used to control the proposed inverter circuit. All the experimental results are captured using MDO 3024 at 200-MHz bandwidth. Independent power control of FM and N-FM IC loads is obtained using ON–OFF control. With ON–OFF control, some minimum power is present in the N-FM load due to the absence of control in the negative half cycle. To control power in N-FM load below the minimum value, frequency control is also implemented.

Fig. 9 depicts the simulation and experimental results when both the loads are operated at their respective full powers.

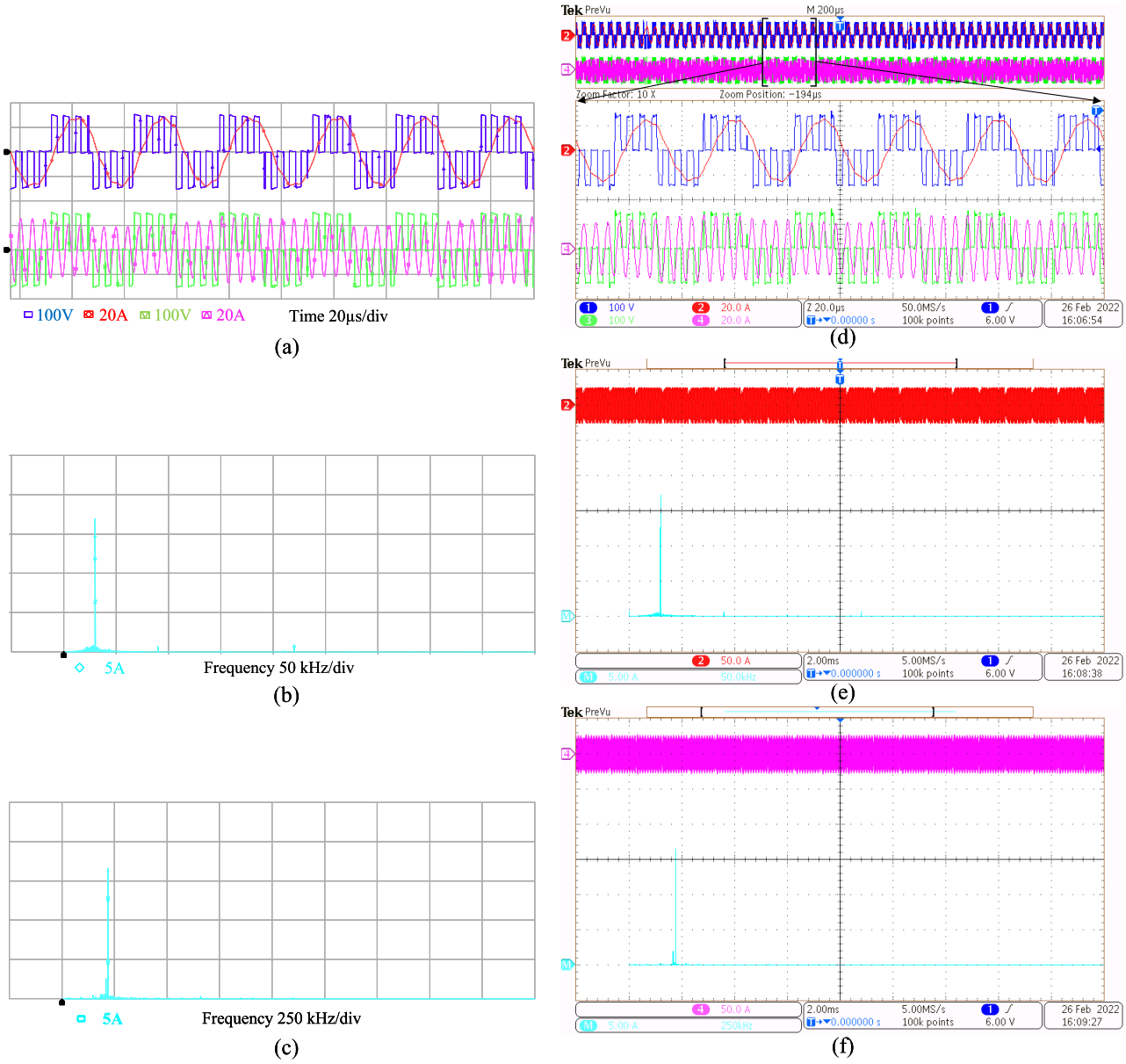

Fig. 9. Simulation and experimentation results when $P_{st} = 838$ W and $P_{al} = 786$ W. (a) and (d) Respectively simulation and experimental voltage-current waveforms of steel and aluminum loads, (b) and (e) simulation and experimental FFTs of steel load current, and (c) and (f) simulation and experimental FFTs of aluminum load current.

Duty cycles for both loads are at 99%. The current flowing through the steel load is 17.3 A, while that of the aluminum load is 16.75 A. Steel load is powered at 838 W and aluminum load is powered at 786 W. The total output power delivered by the inverter circuit is 1624 W. Fig. 9(a)–(c) show the simulation results while Fig. 9(d)–(f) show experimental results. Fig. 9(a) and (d) show the output voltage-current waveforms of the loads under simulation and experimentation respectively. Fig. 9(b) and (e) show FFTs of the current flowing through the steel load under simulation and experimentation respectively. Fig. 9(c) and (f) show FFTs of the current flowing through the aluminum load under simulation and experimental conditions respectively.

Fig. 10 shows experimental results when the inverter is delivering total output power of 1253.64 W. Steel load is operated with duty cycle d_1 of 90% and rms current flowing through it is 16.31 A. It is powered at 744.85 W. Aluminum load is operated with a duty cycle d_2 of 30% and rms current flowing through it is 13.48 A. It is powered at 508.79 W. Fig. 10(a) shows the output voltage and load current waveforms for one cycle of ON–OFF control pulses with frequency (f_{st} and f_{al}) of 1 kHz. Fig. 10(b) shows the zoomed-in view of the respective output voltage and load current waveforms during experimentation when both loads are powered simultaneously. Fig. 10(c) shows the zoomed-in view of the experimental output voltage and load current waveforms. It indicates the state when the series switch for steel load (S_5) is on but the series switch for aluminum load (S_6) is off. Fig. 10(d) shows a zoomed-in view of the waveforms when series switches of both the loads are off.

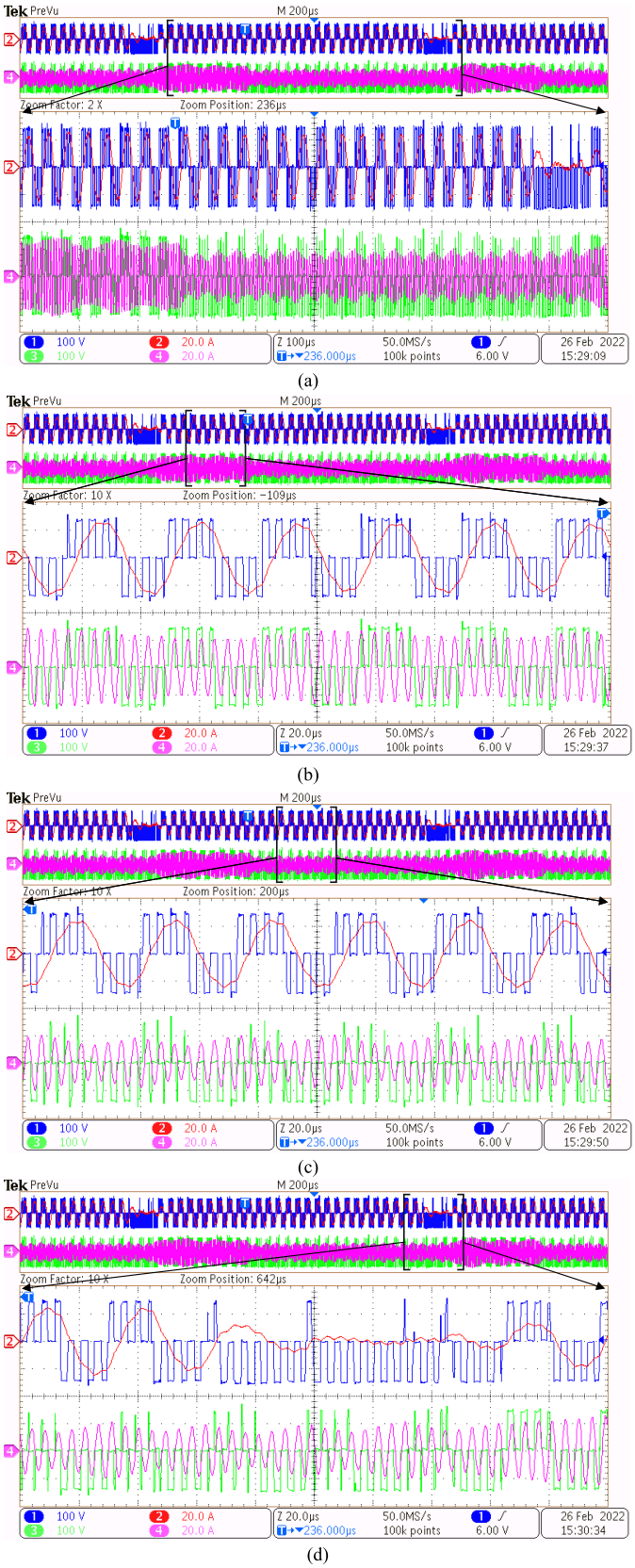

Fig. 10. Experimental voltage-current waveforms of steel and aluminum loads when P_{st} = 744.85 W and P_{al} = 508.79 W. Zoomed view for (a) one control cycle, (b) when S_5 and S_6 are ON, (c) when only S_5 is ON and (d) when S_5 and S_6 are OFF.

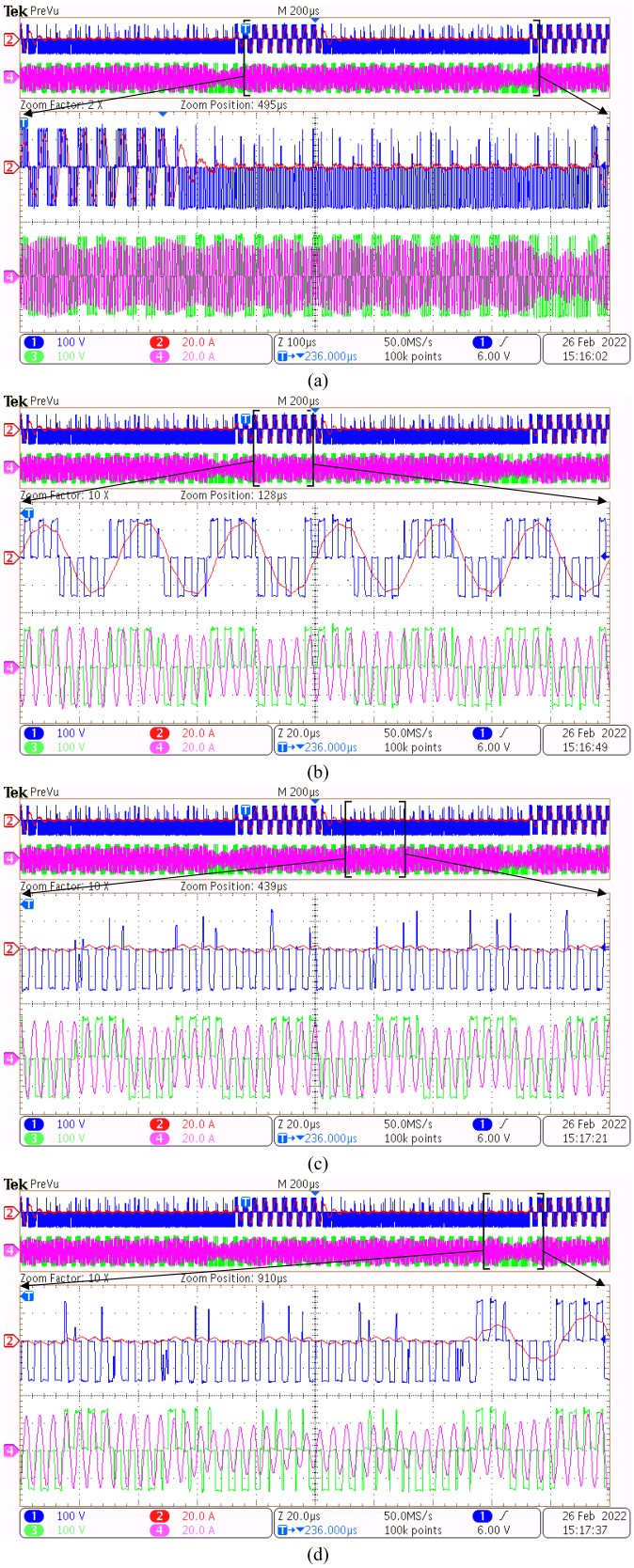

Fig. 11. Experimental voltage-current waveforms of steel and aluminum loads when P_{st} = 261.28 W and P_{al} = 526.3 W. Zoomed view for (a) one control cycle, (b) when S_5 and S_6 are ON, (c) when only S_6 is ON and (d) when S_5 and S_6 are OFF.

Fig. 11 shows the experimental results of the inverter circuit when d_1 is 30% and d_2 is 90%. The rms values of the currents flowing through steel and aluminum loads are 9.66 and 13.71 A respectively. Steel and aluminum loads are controlled at powers of 261.28 and 526.3 W respectively. Fig. 11(a) shows the voltage-current waveforms of the loads for one cycle

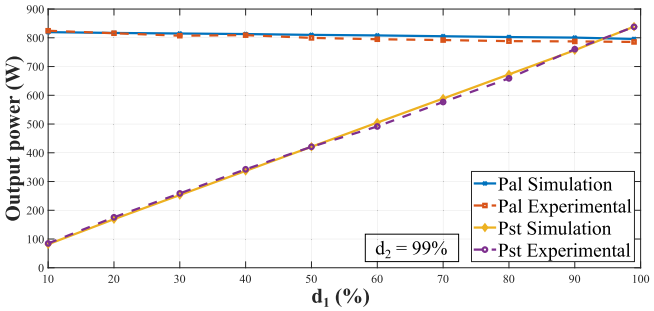

Fig. 12. Output power variation with d_1.

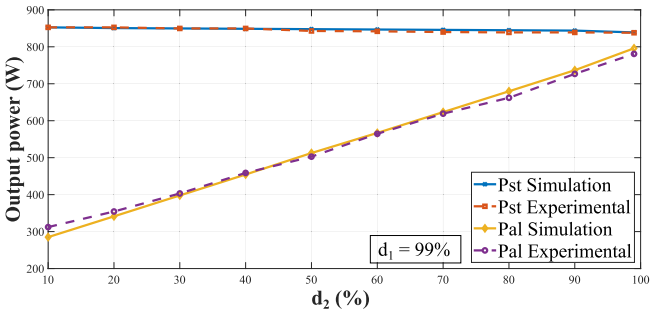

Fig. 13. Output power variation with d_2.

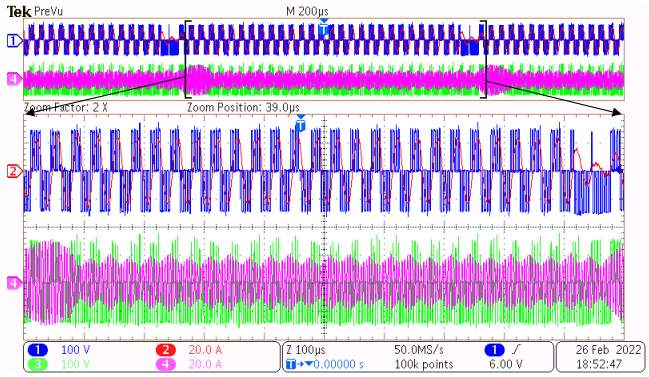

Fig. 14. Experimental voltage-current waveforms for steel and aluminum loads at 220 kHz with $d_1 = 95\%$ and $d_2 = 10\%$.

of ON–OFF control. Fig. 11(b) shows the zoomed-in view of voltage-current waveforms when both the series switches are on. Fig. 11(c) shows the zoomed-in view of voltage-current waveforms when series switch of the steel load is off while that of aluminum load is on. Fig. 11(d) shows the zoomed-in view of voltage-current waveforms when both the series switches are in OFF-state.

The variation in output power with ON–OFF control is plotted in Figs. 12 and 13. Fig. 12 shows the simulation and experimental results when the output power is varied over d_1 by keeping d_2 constant at 99%. By varying d_1 from 10% to 99%, steel load power is varied from 84.7 to 838 W while aluminum load power remains almost constant at its maximum value. Fig. 13 shows the simulation and experimental results when the output power is varied over d_2 keeping d_1 constant at 99%. By varying d_2 from 10% to 99%, aluminum load power is varied from 312.24 W to 786 W while steel load power remains almost constant at its maximum value. Linear

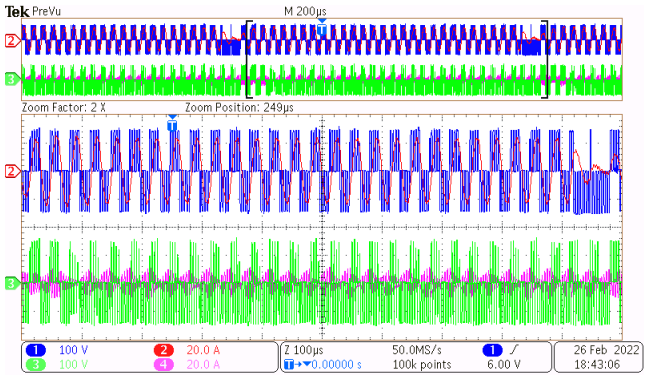

Fig. 15. Experimental voltage-current waveforms for steel and aluminum loads at 234 kHz when $d_1 = 95\%$ and $d_2 = 10\%$.

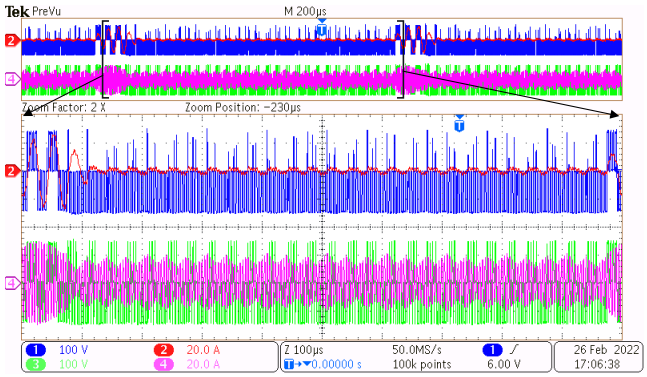

Fig. 16. Experimental voltage-current waveforms for steel and aluminum loads at 220 kHz with $d_1 = 10\%$ and $d_2 = 10\%$.

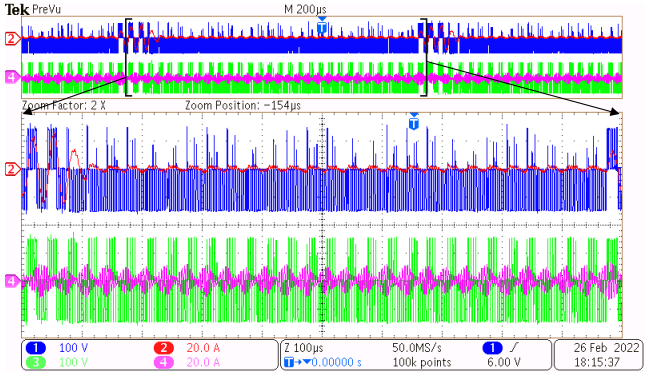

Fig. 17. Experimental voltage-current waveforms for steel and aluminum loads at 234 kHz with $d_1 = 10\%$ and $d_2 = 10\%$.

power control for both loads is independently obtained by using ON–OFF control as shown in these graphs.

The experimental results for frequency based control of aluminum load when $d_1 = 95\%$ and $d_2 = 10\%$ are shown in Figs. 14 and 15. Fig. 14 shows experimental output voltage-current waveforms when leg-2 is operated at 220 kHz. The rms current flowing through steel and aluminum loads are 17 and 10 A respectively. Steel load is powered at 809.2 W and aluminum load is controlled at 280 W. Fig. 15 shows the experimental waveforms for output voltage and load current when control frequency is 234 kHz. The rms current flowing through steel and aluminum loads are 17.12 and 5.01 A respectively. Steel load is powered at 820 W and aluminum load is

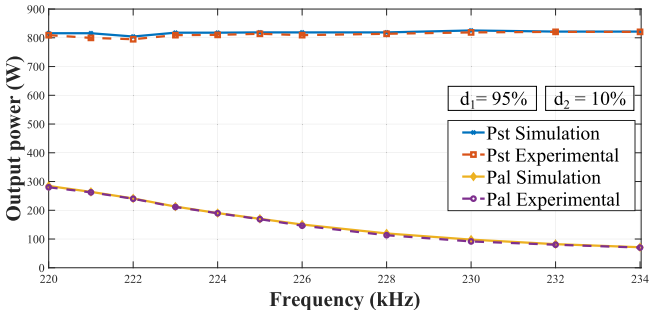

Fig. 18. Output power variation with high frequency when $d_1 = 95\%$ and $d_2 = 10\%$.

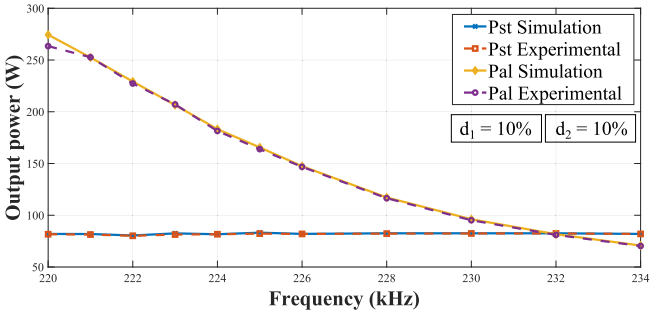

Fig. 19. Output power variation with high frequency when $d_1 = 10\%$ and $d_2 = 10\%$.

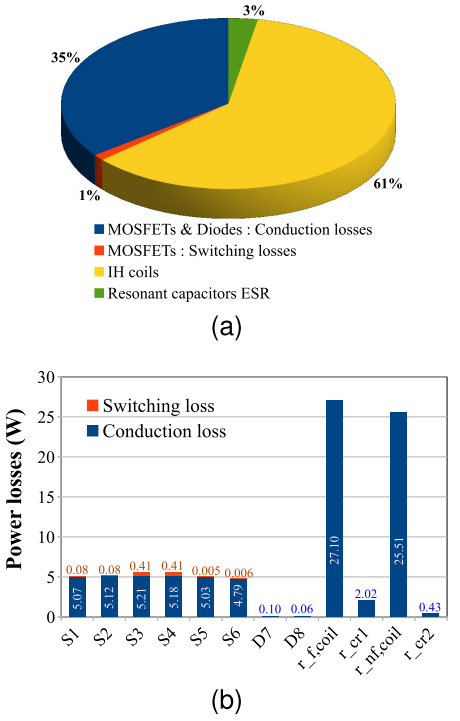

Fig. 20. Loss analysis of the proposed inverter when $d_1 = d_2 = 99\%$. (a) Power loss diagram. (b) Componentwise power loss distribution.

controlled at 70.28 W. Figs. 16 and 17 show the experimental voltage-current waveforms for steel and aluminum load. Both the loads are operated with a duty cycle of 10% i.e., $d_1 = d_2 = 10\%$. Fig. 16 shows waveforms when the steel load current is 5.4 A, powering it at 81.65 W and the aluminum load current is 9.7 A, controlling it at 263.45 W. Fig. 17 shows waveforms when the steel load current is 5.41 A, powering it at 81.95 W and the aluminum load current is 5.01 A, controlling it at 70.28 W. From simulation and experiment based results, it can be noted that both are in good accord with each other. It shows independent power control in steel and aluminum loads using ON–OFF control. The power control range for aluminum load is increased by incorporating frequency based control.

The frequency control for aluminum load is depicted in Figs. 18 and 19. Fig. 18 shows the output power versus frequency graph for simulation and experimentation results when $d_1 = 95\%$ and $d_2 = 10\%$. The aluminum load power varies from 280 W to 70.28 W as leg-2 (S_3, S_4) frequency is varied from 220 to 234 kHz. The power in the steel load reports a small variation from 809.2 to 820 W. It can be observed that steel load power is maintained almost constant during the entire range of aluminum load power control. Fig. 19 shows the output power variation over frequency when $d_1 = 10\%$ and $d_2 = 10\%$. The curves related to simulation and experimental results are plotted in this graph. The aluminum load power varies from 263.45 to 70.28 W as leg-2 (S_3, S_4) frequency is varied from 220 to 234 kHz. The power in the steel load has a small variation from 81.65 to 81.95 W. It can be observed that steel load power is maintained almost constant during the entire range of aluminum load power control. Simulation and experimental data for both these graphs are in agreement with each other.

TABLE II
COMPARISON OF PROPOSED INVERTER WITH MLIS

Sl. No.	N_L	N_{DC}	N_S	N_D	N_C	TSV	$\eta_m(\%)$	$P_o(W)$
[21]	15	3	9	4	3	$30.9V_{dc}$	94.10	113.75
[22]	9	2	8	8	0	$22V_{dc}$	97.86	951.91
[23]	9	1	10	4	4	$8.5V_{dc}$	98.03	583.91
[24]	17	1	13	6	4	$11.25V_{dc}$	96.32	1150
[25]	17	1	16	10	4	$23.5V_{dc}$	96.5	434.7
Proposed	3	1	6	2	1	$8V_{dc}$	94.30	1624

Note: N_L= number of output voltage levels, N_{DC}= number of DC sources, N_S= number of switches, N_D= number of diodes, N_C= number of capacitors, TSV(total standing voltage) = blocking voltage of each switching device × number of switching devices, η_m= maximum efficiency and P_o= respective rated power.

A. Loss Analysis

The power loss analysis of the proposed inverter is carried out using PSIM software [15]. Simulation has been performed at the same operating condition as the experimental condition. The MOSFETs and diodes are modeled as per the parameters mentioned in the respective datasheets. Equivalent series resistance (ESR) of the resonant capacitors and parasitic resistance of IH coils has been measured using NumetriQ phase-sensitive multimeter-PSM 1735. The parameters used for simulation are mentioned in Table I. The detailed loss analysis of the proposed inverter for full load operation ($d_1 = d_2 = 99\%$) is presented in Fig. 20. Fig. 20(a) shows the power loss diagram for the inverter and Fig. 20(b) shows the componentwise power loss distribution. It can be observed that the majority of power loss takes place in IH coils due to their parasitic resistances. As ZVS is achieved during turn-on, the switching losses are negligible for the proposed inverter.

TABLE III
COMPARISON OF THE IH INVERTERS SUITABLE FOR FM AND N-FM LOADS

Sl. No.	No. of switches	Operating frequency (kHz)	Peak efficiency (%)	Control technique used	Control complexity	Independent/ simultaneous control	Additional no. of switches per load (>2 loads)
[10]	2	23-75	96	Selective harmonic, non-linear	Less	Yes/No	2 + relay
[15]	4	25-125	96.5	LAM, non-linear	High	Yes/No	4 + relay
[19]	4	30 & 150	92	ADC, non-linear	Less	Yes/Yes	2
[18]	8	20,100,400	≥92	ADC, non-linear	Moderate	Yes/Yes	2
[16]	4	30/78	94.32	PWM + PSC, non-linear	Moderate	Yes/No	4 + relay
Proposed	6	30 & 220	94.3	ON-OFF, linear	Less	Yes/Yes	1 + diode

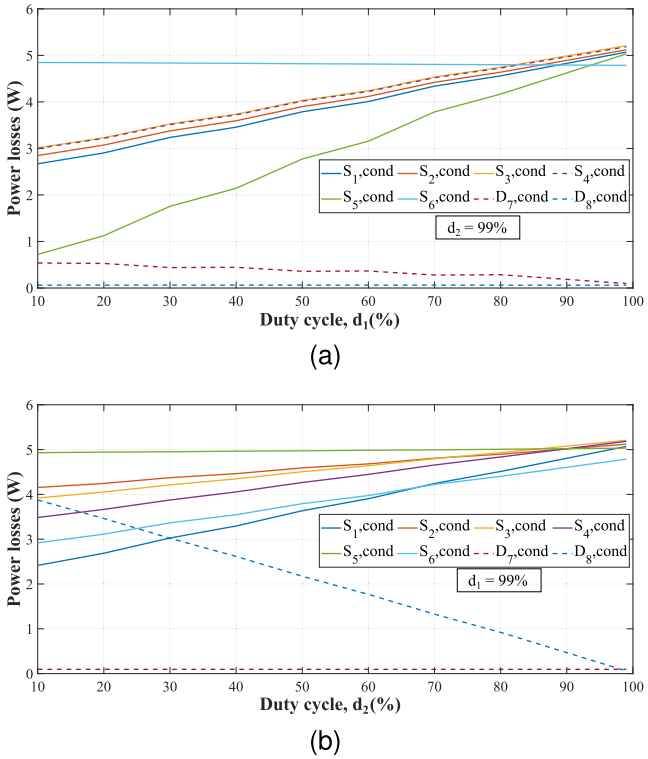

Fig. 21. Conduction power loss in switching devices over duty cycle control. (a) P_{st} is varied while P_{al} is controlled at 786 W. (b) P_{al} is varied while P_{st} is controlled at 838 W.

Fig. 21 depicts the variation of conduction loss in switching devices with duty cycle. Fig. 21(a) shows the conduction loss when $d_2 = 99\%$ and d_1 is varied from 10% to 99%. Conduction losses in MOSFETs $S_1(S_{1,\text{cond}})$, $S_2(S_{2,\text{cond}})$, $S_3(S_{3,\text{cond}})$, $S_4(S_{4,\text{cond}})$ and $S_5(S_{5,\text{cond}})$ increase linearly. As S_6 is continuously on, the power losses in it remains constant while it is negligible in D_8. The losses in D_7 decrease linearly as d_1 is increased. Fig. 21(b) shows the conduction loss when $d_1 = 99\%$ and d_2 is varied from 10% to 99%. The conduction losses in S_1, S_2, S_3, S_4 and S_6 increase linearly. As S_5 is continuously on, the power losses in it remain constant while it is negligible in D_7. The losses in D_8 decrease linearly as d_2 is increased. From Fig. 21(a) and (b), it can be noted that conduction losses in D_8 are relatively more when compared to D_7. This is because when S_5 is off, the FM load current decays to zero. On the contrary, when S_6 is off, some minimum current continues to flow as explained in the operating modes which lead to more conduction losses in diode D_8.

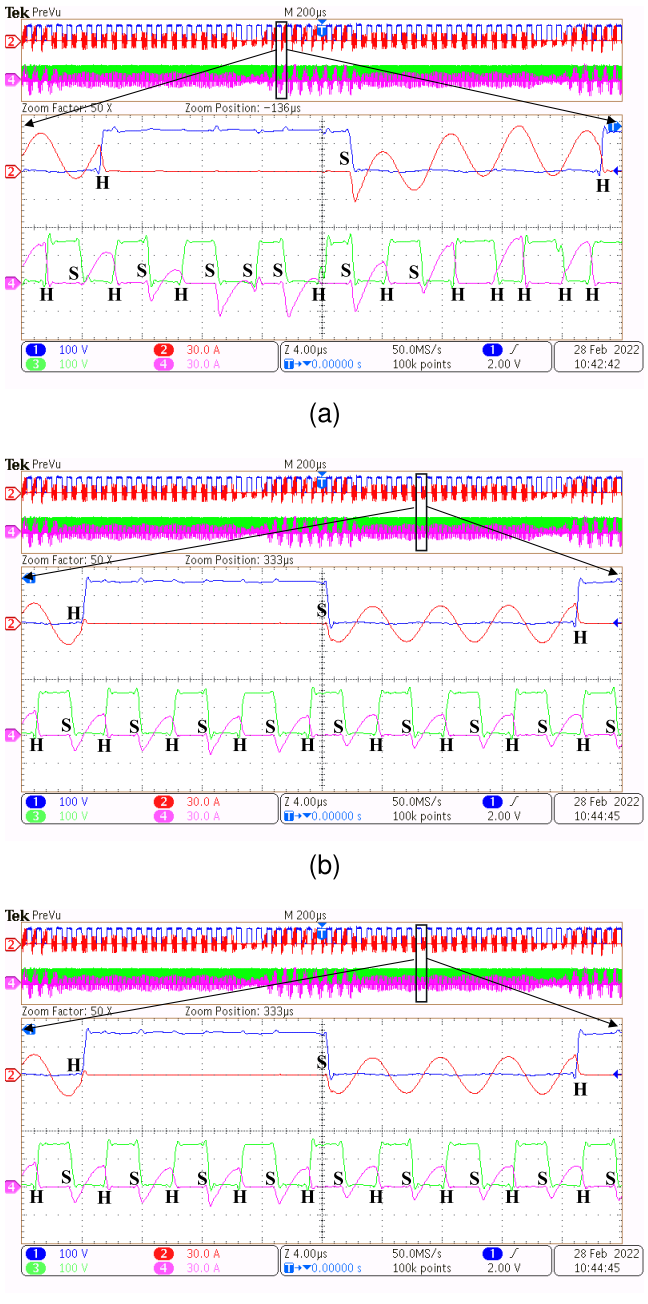

Fig. 22. From top to bottom: voltages and currents of switching devices S_1 and S_4. S: soft switching, H: hard switching. (a) S_5 and S_6 are on. (b) S_5 is off and S_6 is on. (c) S_5 and S_6 are off.

The voltages and currents of switching devices S_1 and S_4 with $d_1 = 30\%$ and $d_2 = 90\%$ are shown in Fig. 22.

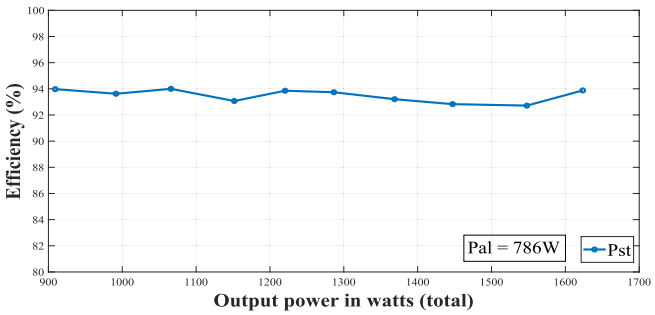

Fig. 23. Efficiency versus output power. P_{st} is varied while P_{al} is controlled at 786 W.

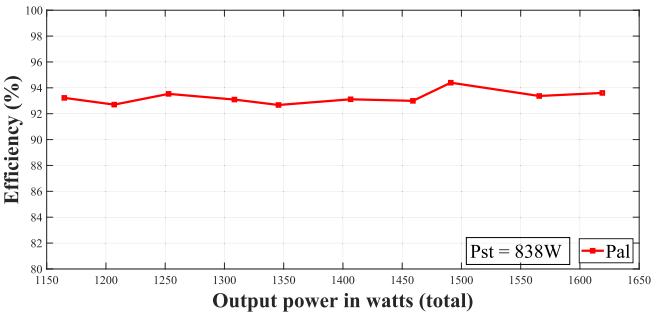

Fig. 24. Efficiency versus output power. P_{al} is varied while P_{st} is controlled at 838 W.

The soft switching (S) and hard switching (H) transitions are also indicated. It can be observed that due to lagging nature of load currents, soft switching (ZVS) is obtained during turn-on for most of the switching transitions. Hence, switching losses due to turn-on of devices can be ignored. Hard switching is present during turn-off of the switching devices. As the proposed inverter operation is similar to a combination of two half bridges operating at high and low frequencies, the turn-off losses can be derived using a detailed explanation given in [26]. Hence, the turn-off losses can be evaluated as follows:

$$P_{\_\text{off}} = f_{\text{hf}} V_{\text{dc}} I_{\text{off,hf}} \left(\frac{2t_{r,\text{hf}}}{3} + t_{f,\text{hf}} \right) + f_{lf} V_{\text{dc}} I_{\text{off},lf} \left(\frac{2t_{r,lf}}{3} + t_{f,lf} \right) \quad (17)$$

where, f_{hf} and f_{lf} are high and low switching frequencies respectively. $I_{\text{off,hf}}$ and $I_{\text{off},lf}$ are turn-off currents of switching devices of high-frequency and low-frequency legs respectively. The $t_{r,\text{hf}}$ and $t_{r,lf}$ are rise time for the device voltage of high- and low-frequency legs respectively. The $t_{f,\text{hf}}$ and $t_{f,lf}$ are the device current fall times of high- and low-frequency legs, respectively.

The efficiency of the proposed inverter over the entire power range is shown in Figs. 23 and 24. Fig. 23 depicts the efficiency versus steel load power while keeping aluminum load power constant at its maximum value of 786 W. It is observed that inverter efficiency is high which is around 94% for a wide range of output power. Fig. 24 shows the efficiency versus aluminum load power with keeping steel load power at its maximum value of 838 W. It is observed that inverter efficiency is high which is around 93% for a wide range of output power. Hence, the proposed inverter offers more than 92.5% efficiency over the entire power control range and also a peak efficiency of 94.3%. The efficiency is evaluated as the ratio of output power ($I^2_{f,\text{rms}} R_f + I^2_{\text{nf,rms}} R_{\text{nf}}$) to input power ($V_{\text{dc}} I_{\text{dc}}$). Fig. 25 shows thermal images for steel and aluminum load when they are operated at 60% and 90% duty cycles respectively for a minute.

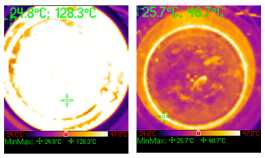

Fig. 25. Thermal images for the steel and aluminum loads at $d_1 = 60\%$ and $d_2 = 90\%$ respectively.

B. Comparison of the Proposed Inverter With Existing Inverters

For dc-ac application, highly efficient multilevel inverters (MLIs) with reduced component count were proposed in [21], [22], [23], [24], [25]. The detailed comparison is provided in Table II. These MLIs offer high efficiency but their output voltage frequency is low (50–60 Hz). Hence, they are not suitable for IH applications. The features of the proposed inverter have also been compared with the recently proposed inverter topologies available in the literature which are suitable for FM and N-FM IH loads. The comparison is described in Table III. In [10], [15] and [16] the authors' primary objective is to propose a universal IH solution i.e., one vessel at a time (FM or N-FM). Khatroth and Shunmugam [18] and Papani et al. [19] aimed for heating FM and N-FM loads simultaneously i.e., multiple load IH solutions. It can be observed from Table III that the above-mentioned inverter topologies use nonlinear control which is not desirable. Some of them do not offer simultaneous operation and control of IH loads. In some of the proposed topologies, control is more involved. Also, extension for multiple loads (more than 2) leads to an increase in component count and hence size of the solution. The proposed inverter can be easily extended for more loads by the addition of a series switch and a diode per IH load. It also offers linear, independent, and simultaneous control for all IH loads.

V. Conclusion

An inverter circuit for heating vessels of different materials with ON–OFF control for multiload application is proposed in this article. For both the different material loads, linear power variation is obtained using ON–OFF control independently. The range of power control for an aluminum load has been increased by implementing frequency-based control. The operation of the proposed inverter has been validated through simulation and experiments. The designed experimental prototype has been tested for a total output power of 1624 W. It offers higher efficiency over the entire range of power control. Performance comparison of the proposed inverter is presented in Table III. Simple, linear, simultaneous,

and independent power control in vessels of different material are key advantages of the proposed inverter circuit for multiple load IC application. It can also be used for heating more number of loads by adding a low-frequency series switch and a diode combination per load which makes it suitable for multiload IC applications.

REFERENCES

[1] O. Jimenez, O. Lucia, I. Urriza, L. A. Barragan, P. Mattavelli, and D. Boroyevich, "An FPGA-based gain-scheduled controller for resonant converters applied to induction cooktops," *IEEE Trans. Power Electron.*, vol. 29, no. 4, pp. 2143–2152, Apr. 2014.

[2] Ó. Lucía, P. Maussion, E. J. Dede, and J. M. Burdío, "Induction heating technology and its applications: Past developments, current technology, and future challenges," *IEEE Trans. Ind. Electron.*, vol. 61, no. 5, pp. 2509–2520, May 2014.

[3] J.-E. Yeon, K.-M. Cho, and H.-J. Kim, "A 3.6 kW single-ended resonant inverter for induction heating applications," in *Proc. 17th Eur. Conf. Power Electron. Appl. (EPE ECCE-Europe)*, Sep. 2015, pp. 1–7.

[4] S. Llorente, F. Monterde, J. M. Burdio, and J. Acero, "A comparative study of resonant inverter topologies used in induction cookers," in *Proc. APEC. 17th Annu. IEEE Appl. Power Electron. Conf. Expo.*, Mar. 2002, pp. 1168–1174.

[5] D. N. Sankhe, R. R. Sawant, and Y. S. Rao, "FPGA-based hybrid control strategy for resonant inverter in induction heating applications," *IEEE J. Emerg. Sel. Topics Ind. Electron.*, vol. 3, no. 1, pp. 156–165, Jan. 2022.

[6] P. K. Jain, A. St-Martin, and G. Edwards, "Asymmetrical pulse-width-modulated resonant DC/DC converter topologies," *IEEE Trans. Power Electron.*, vol. 11, no. 3, pp. 413–422, May 1996.

[7] J. M. Burdio, L. A. Barragan, F. Monterde, D. Navarro, and J. Acero, "Asymmetrical voltage-cancellation control for full-bridge series resonant inverters," *IEEE Trans. Power Electron.*, vol. 19, no. 2, pp. 461–469, Mar. 2004.

[8] V. Esteve et al., "Optimal LLC inverter design with SiC MOSFETs and phase shift control for induction heating applications," *IEEE Trans. Ind. Electron.*, vol. 69, no. 11, pp. 11100–11111, Nov. 2022.

[9] B. Salvi, N. Vishwanathan, and S. Porpandiselvi, "A direct AC–AC multiple load inverter for vessels of different materials," in *Proc. Nat. Power Electron. Conf. (NPEC)*, Dec. 2021, pp. 1–6.

[10] I. Millan, J. M. Burdío, J. Acero, O. Lucía, and S. Llorente, "Series resonant inverter with selective harmonic operation applied to all-metal domestic induction heating," *IET Power Electron.*, vol. 4, no. 5, pp. 587–592, May 2011.

[11] T. Tanaka, "A new induction cooking range for heating any kind of metal vessels," *IEEE Trans. Consum. Electron.*, vol. 35, no. 3, pp. 635–641, Aug. 1989.

[12] H. Yonemori and M. Kobayashi, "On the heating characteristic and magnetic flux of a double-coil drive type induction heating cooker," in *Proc. 32nd Annu. Conf. IEEE Ind. Electron.*, Nov. 2006, pp. 2488–2493.

[13] W. Han, K. T. Chau, C. Jiang, and W. Liu, "All-metal domestic induction heating using single-frequency double-layer coils," *IEEE Trans. Magn.*, vol. 54, no. 11, pp. 1–5, Nov. 2018.

[14] T. Hirokawa, E. Hiraki, T. Tanaka, M. Okamoto, and M. Nakaoka, "The practical evaluations of time-sharing high-frequency resonant soft-switching inverter for all metal IH cooking appliances," in *Proc. 38th Annu. Conf. IEEE Ind. Electron. Soc.*, Oct. 2012, pp. 3302–3307.

[15] H.-P. Park and J.-H. Jung, "Load-adaptive modulation of a series-resonant inverter for all-metal induction heating applications," *IEEE Trans. Ind. Electron.*, vol. 65, no. 9, pp. 6983–6993, Sep. 2018.

[16] W. Han, K. T. Chau, W. Liu, X. Tian, and H. Wang, "A dual-resonant topology-reconfigurable inverter for all-metal induction heating," *IEEE J. Emerg. Sel. Topics Power Electron.*, vol. 10, no. 4, pp. 3818–3829, Aug. 2022.

[17] R. C. M. Gomes, M. A. Vitorino, D. A. Acevedo-Bueno, and M. B. D. R. Correa, "Multiphase resonant inverter with coupled coils for AC–AC induction heating application," *IEEE Trans. Ind. Appl.*, vol. 56, no. 1, pp. 551–560, Jan. 2020.

[18] S. Khatroth and P. Shunmugam, "Cascaded full-bridge resonant inverter configuration for different material vessel induction cooking," *IET Power Electron.*, vol. 13, no. 19, pp. 4428–4438, Dec. 2020.

[19] S. K. Papani, V. Neti, and B. K. Murthy, "Dual frequency inverter configuration for multiple-load induction cooking application," *IET Power Electron.*, vol. 8, no. 4, pp. 591–601, Apr. 2015.

[20] H. Fujita and H. Akagi, "Pulse-density-modulated power control of a 4 kW, 450 kHz voltage-source inverter for induction melting applications," *IEEE Trans. Ind. Appl.*, vol. 32, no. 2, pp. 279–286, Mar. 1996.

[21] S. Majumdar, B. Mahato, and K. C. Jana, "Implementation of an optimum reduced components multicell multilevel inverter (MC-MLI) for lower standing voltage," *IEEE Trans. Ind. Electron.*, vol. 67, no. 4, pp. 2765–2775, Apr. 2020.

[22] S. Paul, K. C. Jana, S. Majumdar, P. K. Pal, and B. Mahato, "Performance analysis of a multimodule staircase (MM-STC)-type multilevel inverter with reduced component count and improved efficiency," *IEEE J. Emerg. Sel. Topics Power Electron.*, vol. 10, no. 6, pp. 6619–6633, Dec. 2022.

[23] P. K. Pal, K. C. Jana, P. Y. Siwakoti, S. Majumdar, and F. Blaabjerg, "An active-neutral-point-clamped switched-capacitor multilevel inverter with quasi-resonant capacitor charging," *IEEE Trans. Power Electron.*, vol. 37, no. 12, pp. 14888–14901, Dec. 2022.

[24] S. Majumdar, K. C. Jana, P. K. Pal, A. Sangwongwanich, and F. Blaabjerg, "Design and implementation of a single-source 17-level inverter for a single-phase transformer-less grid-connected photovoltaic systems," *IEEE J. Emerg. Sel. Topics Power Electron.*, vol. 10, no. 4, pp. 4469–4485, Aug. 2022.

[25] S. Majumdar, B. Mahato, and K. C. Jana, "Analysis and implementation of a generalised switched-capacitor multi-level inverter having the lower total standing voltage," *IET Power Electron.*, vol. 13, no. 17, pp. 4031–4042, Dec. 2020.

[26] M. K. Kazimierczuk and D. Czarkowski, *Resonant Power Converters*. Hoboken, NJ, USA: Wiley, 2012.

Bhavin Salvi received the B.E. degree in electrical engineering from Birla Vishwakarma Mahavidyalaya, Gujarat, India, in 2013, and the M.Tech. degree in power electronics and drives from the National Institute of Technology Warangal, India, in 2018, where he is currently pursuing the Ph.D. degree.

His main research interests include power electronics converter development and digital control for induction heating system, LED lighting system, and maximum power point tracking in photovoltaic based applications.

S. Porpandiselvi (Member, IEEE) received the B.E. degree in electrical and electronics engineering from the Thiagarajar College of Engineering, Madurai, India, in 1996, the M.E. degree in applied electronics from Madurai Kamaraj University, India, in 2001, and the Ph.D. degree in electrical engineering from the National Institute of Technology Warangal, Warangal, India, in 2014.

She is currently working as an Associate Professor with the Department of Electrical Engineering, National Institute of Technology Warangal. Her research interests include high frequency inverters for induction heating applications, resonant converters, LED driver circuits, and PV based applications.

N. Vishwanathan received the B.Sc. (Engg.) degree in electrical engineering from the Dayalbagh Educational Institute, Agra, India, in 1990, the M.Tech. degree in electrical machines and industrial drives from the Regional Engineering College Warangal, Warangal, India, in 1992, and the Ph.D. degree from the Indian Institute of Science, Bengaluru, India, in 2004.

He is currently working as a Professor with the Department of Electrical Engineering, National Institute of Technology Warangal, Warangal. His areas of interest are switched mode power conversion, LED lighting, and electrical drives.